Chap. 10 In "Biomechanics of Living Organs", Ed. Yohan Payan, Jacques Ohayon, Aca. Press, Elsevier, 2017

Non linear Biomechanical Model of the Liver

Stéphanie Marchesseau[a], Simon Chatelin[b], Hervé Delingette[c]

[a] *Clinical Imaging Research Centre, A*STAR-NUS, Singapore*
[b] *ICube, University of Strasbourg, UMR 7357 CNRS, Strasbourg, France*
[c] *Université Côte d'Azur, Inria, Asclepios Team, France*

1. Introduction: Clinical Context

The liver is among the largest organs of the human body with an approximate weight of around 1.5 kg for adults. The biomechanical behavior of this massive soft organ has been studied primarily in the context of car injury (Untaroiu et al., 2015a). Indeed, liver injuries, such as capsule laceration and parenchyma damage, are frequently caused by both frontal and side collisions and are associated with high morbidity and mortality rates. The numerous related rheological and simulation studies are therefore performed in a regime of large deformations and high strain rates, and focus on the mechanisms of tissue failure.

The biomechanics of the liver has also been studied in the context of small strain rates for medical applications, such as computer-aided diagnosis, therapy guidance, therapy training, and therapy planning. For example, in the context of therapy training, several existing surgery simulators (Nickel et al., 2015) aim at training young surgeons to perform the resection of the gall bladder (cholecystectomy) using minimally invasive surgery. Since the gall bladder sits beneath the right lobe of the liver, those simulators often include a simplified real-time model (Delingette and Ayache, 2004) of the liver mechanics. There exist several possible therapies that can be performed on the liver related to the presence of hepatic metastases, often caused by colorectal cancer, or primary tumors, such as hepatocellular carcinoma. Among those procedures, the partial resection of the liver aims at removing functional regions of the liver that include some tumor lesions. Prior to this surgery, liver biopsies are often performed to examine the nature of the tissue at risk. In both cases, the physician must face the issue of properly localizing the lesions based on preoperative imaging (CT or MR images) and intraoperative images (often ultrasound images). Additional guidance can be provided to the surgeon by registering the liver shape from its preoperative configuration to its intraoperative one based on a biomechanical model. In such cases (Oktay et al., 2013; Simpson et al., 2012), the mechanical model must cope with large displacement (finite strain) and acts as a data regularizer to constrain the space of deformations. Such a bio-inspired image registration approach was further used to plan the trajectory of biopsy needle in the liver (Kobayashi et al., 2012), to perform augmented reality to visualize tumor locations during laparoscopic surgery (Plantefève et al., 2015; Haouchine et al., 2015) and to simulate the injection of gas inside the abdominal cavity (pneumoperitoneum) (Bano et al., 2012) (Fig. 1).

2. Anatomy of the Liver

The liver is the heaviest internal organ of the human body. It has an average length, height, and thickness of, respectively 28, 16, and 8 cm. The liver is involved in many physiological

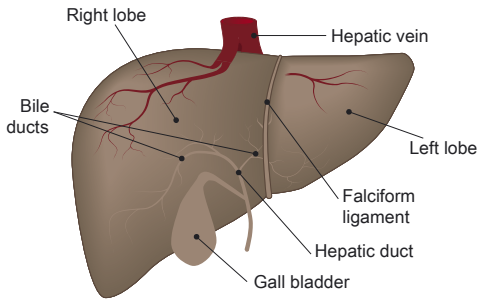

Figure 1: Liver Anatomy including the right and left lobes separated by the falciform ligament.

functions, such as the detoxification of metabolites, the secretion of hormones and proteins, the regulation of glycogen, and the filtering of venous blood to remove toxins.

Three types of blood vessels are located inside the liver: the hepatic artery bringing arterial blood (25% of the flow), the portal vein conveying blood from the digestive tract to be detoxified (75% of the flow), and the subhepatic veins collecting the filtered blood and draining into the inferior veina cava. The bile ducts carry the bile secreted inside the liver into the gallbladder through the cystic duct and to the pancreas through the common bile duct. The portal vein, hepatic artery, and common bile duct jointly enter the liver through a central area called the hepatic hilum.

The liver is separated into a right and left lobe by the falciform ligament, and the Couinaud classification further divides the liver into eight segments. The liver consists of around one million lobules, hexagonal cylindrical structures 0.8-2mm in diameter. Each lobule, which constitutes the basic functional unit of the liver, is made of millions of hepatic cells (hepatocytes) connected to the arterial and the two venous trees. The homogeneous spread of lobules and the amount of blood stored within the liver (about 450mL of blood or 10% of the body's blood volume) explain that the mechanical behavior of the liver parenchyma can be assimilated at a certain scale to that of a porous medium. However, the global mechanical behavior of the liver is also impacted by the presence of its inner fibrous coat known as the Glisson capsule, which ensheaths the veins, arteries, and ducts within the organ.

In terms of mechanical boundary conditions, the liver is maintained in the abdomen through a two-layered fibrous membrane (peritoneum) that encases the liver except in a region where it connects directly to the diaphragm. Furthermore, several ligaments, including the falciform and coronary ligaments, connect the liver to the diaphragm. The portal, arterial, and biliary trees and the hepatic venous tree also play an important role in maintaining the liver in the abdominal cavity.

To conclude, the liver is a fairly complex organ to characterize mechanically because of its multiple components (lobules, blood, capsule) and its soft boundary conditions. The liver of a specific subject can be three-dimensionally reconstructed from CT scan or MR imaging. The injection of contrast agent during multiphase CT imaging allows observation of the arterial and venous trees and detection of the potential presence of lesions.

3. Finite Element Models and Constitutive Laws of the Liver: Literature Review

In addition to the definition of the geometric domain of the liver and its boundary conditions, it is necessary to define a suitable constitutive law in order to build a biomechanical finite element model of the liver. In this section, we review the most common nonlinear constitutive laws to model liver tissue behavior. This review is limited to studies with model parameter identification from experimental tests. After referring to the main nonlinear constitutive laws used for the liver tissue, the main physiological properties and their implications in the nonlinear mechanical response are investigated.

3.1. Nonlinear Constitutive Laws for Liver Modeling

The nonlinear models dedicated to biological soft tissues are based on the identification of nonlinear constitutive laws that are defined by a specific strain energy function W. In this section, the different forms of the strain energy functions identified from hepatic tissue tests are exposed and compared under uniaxial loading stress/strain relationship using

$$\mathbf{T} = 2\mathbf{F} \cdot \frac{\partial W}{\partial \mathbf{C}}$$

where **T**, **F** and **C** are the first Piola-Kirchhoff stress tensor (Lagrangian stress), the deformation gradient tensor, and the right Cauchy-Green strain tensor, respectively. The most popular nonlinear constitutive laws are summarized under the assumption of incompressibility in Table 3.1,i.e. assuming that $I_3 = 1$ (**E**, λ, μ, λ_i, I_i being the Green-Lagrange strain tensor, the first and second Lamé coefficients, the principal stretches and the invariants of the the right Cauchy-Green strain tensor for $i = 1, 2, 3$ respectively, k_B, Θ, n and N being the Boltzmann constant, the temperature, the chains density and the number of constitutive rigid links of the chains, respectively).

Table 1 Main Nonlinear Constitutive Laws Identified to Model the Liver Tissue

Polynomial forms	
Neo-Hookean	$W = C_1(I_1 - 3)$
Mooney-Rivlin (generalized)	$W = \sum_{i+j>0}^{N} C_{ij}(I_1 - 3)^i (I_2 - 3)^j$
Ogden	$W = \sum_{k=1}^{N} \frac{\mu_k}{\alpha_k}(\lambda_1{}^{\alpha_k} + \lambda_2{}^{\alpha_k} + \lambda_3{}^{\alpha_k} - 3)$
Bogen	$W = \frac{\mu_1}{\alpha_1}(\lambda_1{}^{\alpha_1} + \lambda_2{}^{\alpha_1} + \lambda_3{}^{\alpha_1} - 1)$
Yeoh (reduced polynomial model)	$W = \sum_{k=1}^{N} C_k(I_1 - 3)^k$
Arruda-Boyce	$W = nk_B\theta\left[\frac{1}{2}(I_1 - 3) + \frac{1}{20N}(I_1^2 - 9) + \frac{1}{1050N^2}(I_1^3 - 27) + \frac{1}{7000N^3}(I_1^4 - 81) + \frac{1}{673750N^4}(I_1^5 - 243) + \cdots\right]$
Saint Venant-Kirchhoff	$W = \frac{\lambda}{2}(tr\mathbf{E})^2 + \mu(tr\mathbf{E}^2)$
Exponential and Logarithmic forms	
Fung-Demiray	$W = \frac{C_1}{2C_2}\left(e^{C_2(I_1-3)} - 1\right)$
Logarithmic	$W = -C_1 ln\left(1 - C_2(\lambda_1{}^{\alpha_1} + \lambda_2{}^{\alpha_1} + \lambda_3{}^{\alpha_1} - 3)\right)$
Exponential	$W = C_1\left(e^{C_2(\lambda_1{}^{\alpha_1} + \lambda_2{}^{\alpha_1} + \lambda_3{}^{\alpha_1})} - 1\right)$
Combined forms	
Veronda-Westmann	$W = C_1\left(e^{C_3(I_1-3)} - 1\right) + C_2(I_2 - 3)$

Table 1: Main Nonlinear Constitutive Laws Identified to Model the Liver Tissue

3.1.1. Polynomial hyperelastic models

Polynomial forms of the strain energy are the most popular for the implementation of the liver tissue nonlinear behavior. The neo-Hookean model is the simplest polynomial function, based on the statistical thermodynamic and entropy conservation of cross-linked polymer chains. Hepatic tissue characterization using the neo-Hookean model has been proposed in several studies (Chui et al., 2004; Ahn and Kim, 2010). The Mooney-Rivlin model consists of a generalization of the neo-Hookean model, by the addition of the second invariant of the right Cauchy-Green strain tensor. This model is one of the most-used at different orders to simulate the nonlinear mechanical response of the hepatic tissue ($N = 1$, (Hu and Desai, 2003); $N = 3$, (Chui et al., 2004); $N = 2$, (Umale et al., 2013); $N = 2$, (Fu et al., 2013); $N = 2$, (Fu and Chui, 2014)). However, the neo-Hookean model and the low-order Mooney-Rivlin (up to the second order) alone have been shown to be insufficient to reproduce the entire compression/elongation behavior of the hepatic tissue (Chui et al., 2004). The use of high-order Mooney-Rivlin constitutive laws is thought to result in the identification of negative coefficients, which is not physically valid (Hu and Desai, 2004). Reduced polynomial models (Lister et al., 2011), Bogen (Chui et al., 2004) and Ogden strain functions ($N = 3$, (Hu and Desai, 2004); $N = 2$ to 4, (Gao and Desai, 2010); $N = 4$, (Lister et al., 2011); $N = 1$, (Untaroiu and Lu, 2013); $N = 1$, (Lu et al., 2014); $N = 1$, (Untaroiu et al., 2015b)) have also been largely used, but there is still no clear consensus on which of the polynomial forms models the nonlinear behavior of the hepatic tissue the most accurately.

3.1.2. Exponential and logarithmic hyperelastic models

Exponential and logarithmic constitutive forms have been presented as potential models representing the stress-strain behavior of hepatic tissue at least as well as the simple polynomial strain energy functions for both compression and elongation (Chui et al., 2004). Different formulations of exponential strain energy functions (such as the Fung-Demiray model) have been successfully identified on both the *ex vivo* and *in vivo* (mainly indentation tests) experimental response of hepatic tissue (Carter et al., 2001; Tamura et al., 2002; Brown et al., 2003; Chui et al., 2004; Roan and Vemaganti, 2007; Rosen et al., 2008). Both exponential and logarithmic models show similar capacities to simulate hepatic tissue response (Chui et al., 2004).

3.1.3. Combined models

Combining the different forms of the strain energy functions is thought to result in the improvement of the modeling of hepatic tissue, including high-order polynomial formulations (Chui et al., 2004). The most popular approach consists in combining polynomial with either logarithmic or exponential constitutive laws (Fu et al., 2013; Fu and Chui, 2014), with the possibility of including transverse isotropy using the fourth-strain invariant (Chui et al., 2007). The Veronda-Westmann strain energy function combines an exponential form with a polynomial formulation that includes the second-strain invariant. Initially developed to simulate the skin response, this law has been successfully applied to healthy liver tissue (Yin et al., 2004; Chui et al., 2004).

3.1.4. Inclusion of viscosity and porosity in the non-linear constitutive laws

By modification of the formulations, the influence of viscosity has been included by some of the authors for both the neo-Hookean model (Miller, 2000) and the first-order Mooney-Rivlin model (Liu and Bilston, 2002; Kim and Srinivasan, 2005; Samur et al., 2007). This extension of polynomial forms gives reasonable estimation of the hepatic tissue response at large strains over a large range of strain rates (Liu and Bilston, 2002). Rate dependence can be also added in

a hyperviscoelastic expression of the Ogden formulation by representing the relaxation function of the liver tissue as the Prony's series ($N = 6$, (Sato et al., 2013)). A nonlinear strain-hardening fractional derivative constitutive law has been proposed for liver tissue by Nicolle *et al.* (Nicolle et al., 2010). This approach gives the possibility to simulate the response of the tissue in both the linear and the nonlinear viscoelastic regime over a significant range of compression strains (ranging from 0.01 to 1) and strain rates (ranging from 0.0151 to 0.7 s^{-1}). Another form of constitutive laws consists of the combination of a polynomial, exponential or logarithmic nonlinear strain energy function with viscosity by the incorporation of time-dependence in a simplified integral model (Fung, 1967). While this quasi-linear viscoelastic (QLV) formulation has been used successfully to model the liver (Tamura et al., 2002; Nava et al., 2004; Roan and Vemaganti, 2007; Nava et al., 2008; Jordan et al., 2009), its capability to simulate hepatic tissue at large strains and high strain rates has not yet been fully demonstrated.

In addition to viscosity, the inclusion of porosity in a second-order reduced polynomial model was proposed in 2006 by Kerdok, who used biphasic theory to include flow-independent hyperelasticity (Kerdok, 2006). This approach consisting of considering the liver as a fluid-filled sponge was also proposed by Raghunathan *et al.* in 2010 (Raghunathan et al., 2010). This model was extended by Marchesseau *et al.* in 2010 (Marchesseau et al., 2010) and is further developed in this chapter. While playing a major role in the nonlinear response of the liver, the inclusion of porous components in the constitutive hepatic models is still marginal.

3.2. Influence of the Test Conditions and Specific Mechanical Properties

Some experimental and physiological aspects play a major role in the capability of a constitutive law to model the mechanical response of liver tissue under specific loadings. These characteristics have to be defined carefully and determine not only the choice of the constitutive law but also the choice of the experimental tests to identify the parameters of the rheological model.

3.2.1. From in vitro to in vivo characterizations

In most studies, the nonlinear constitutive laws for the liver have been identified exclusively from *ex vivo* experiments. Owing to its invasiveness, *ex vivo* testing (cut samples or whole organ) is associated with possible limitations and biases (destructive invasive approaches) when compared to *in vivo* physiological states (pressurization, vascularization, moisturizing, *postmortem* degradation, and necrosis). The storage of the specimens is one of the first critical aspects of *in vitro* testing. It has been showed that stiffness of the hepatic tissue increases not only after freezing/thawing (by a factor 1.44-1.68 at 20% of strain after 30 days of frozen storage) but also with increased preservation time (by a factor 1.58-1.96 at 20% of strain after 60 days of frozen storage)(Lu et al., 2014). The local and global failure strains have been shown to decrease significantly with both freezing/thawing and increased storage time. More than 50% and only 17% differences have been observed in steady state stiffness by Ottensmeyer *et al.* (Ottensmeyer, 2002; Kerdok, 2006) between *in vivo* and unperfused liver tissue, and between *in vivo* and perfused hepatic tissue (maintaining temperature, hydration,, and physiologic pressure), respectively. This observation illustrates the fact that perfusion plays a major role in the nonlinear response of the liver, which is often underestimated by the *in vitro* identifications. Moreover, the models identified by these different tests conditions are strongly modified in their time-domain and frequency-domain responses, illustrating the importance of identifying the hepatic nonlinear models on *in vivo* experimental measurements to account for viscosity in the liver hyperelastic models (Jordan et al., 2009; Sato et al., 2013).

Up to now, the *in vivo* techniques used to identify the nonlinear response of the liver tissue consisted either in indentation (Carter et al., 2001; Ottensmeyer, 2002; Hu and Desai, 2004; Kim and Srinivasan, 2005; Samur et al., 2007; Jordan et al., 2009; Ahn and Kim, 2010; Lister et al., 2011) or aspiration (Nava et al., 2004, 2008) or monitorized endoscopic grasper (Rosen et al., 2008). Although maintaining most of the *in vivo* parameters of the physiological environment, these techniques are limited to the local and superficial characterization of the organ and necessitate a direct contact with the liver, making them partially invasive. Magnetic resonance- and ultrasound imaging-based elasticity imaging (referred to as elastography) are the only methods giving the opportunity to identify *in vivo* and noninvasively the mechanical response of the organs (Vappou, 2012). The comparison between *in vivo* elastographic and *ex vivo* rheometric measurements has been investigated (Chatelin et al., 2011). While elastography is a continuously expanding field for diagnostic purpose, it is still limited to the investigation of the linear behavior of soft tissue and cannot yet been used for noninvasive identification of the nonlinear mechanical response of liver tissue.

3.2.2. Dependence to the strain rate

Porosity and viscosity are two characteristics that would both involve a time and frequency dependence in the response of the tissue. In most of the experiments aiming at identifying nonlinear constitutive laws, these properties will be characterized by a strain rate dependence on the medium. By identifying nonlinear models from uniaxial tensile/compression tests on *ex vivo* samples with varying loading rates (strain rates ranging from 0.003 to 0.606 s^{-1}), the effect of strain rate on porcine liver has been shown to be relatively insignificant by Chui *et al.* (Chui et al., 2004). However, by extending the range of strain rates to all values proposed in the literature for the nonlinear characterization of hepatic tissue (ranging from 0.003 to 22.5 s^{-1}), significant effects of the loading speed appear clearly, as reported in Fig.2A (nonlinear models expressed in uniaxial tensile/compression as the first Piola Kirchhoff stress over the stretch ratio). These specificities have been confirmed from nonlinear shear tests showing that the liver tissue has to be considered as a very soft solid or highly viscous fluid (Liu and Bilston, 2002). Tensile tests have shown that the elasticity increases from 58 to 61, 68 and 100 kPa with increasing strain rates from 0.01 to 0.1, 1 and 10 s^{-1}, respectively (Lu et al., 2014). The strain rate dependence affects not only the nonlinear behavior but also the failure stress with average second Piola-Kirchhoff stress values ranging from 33 to 94 kPa for strain rates from 0.01 to 1 s^{-1} (Untaroiu and Lu, 2013). Because of variations in the protocols from the studies reported in Fig.2A, it remains difficult to extract a quantitative description of the strain rate dependency from the literature. One of the easiest way to compare all of these results is to extract the equivalent elasticities at small strain through the chord modulus (equivalent linear behavior between 0% and 10% strain) from this figure and to represent them as function of the strain rate for the different model categories (Fig.2B and C for the models identified from compression and tensile tests, respectively). The same trend is observed in both compression and tensile (named group 1 and group 2, respectively), with a similar stiffening with increased strain rate. Only one group (named group 3) shows lower strain rate dependence, but correspond to studies dealing with modeling of the rupture and nonlinear behavior at large strain only (with Ogden models limited to the first order). One of the most realistic assumption is to consider porosity and viscosity as dependent of loading speed at low and high strain rate values, respectively. Consequently, the strain rate dependence has to be accounted for the nonlinear liver models by means of the inclusion of porosity and viscosity (for the lowest and highest loading rates, respectively) in the constitutive law. The influence of the strain rate is fundamental and is conditioning the nonlinear constitutive law used to simulate the

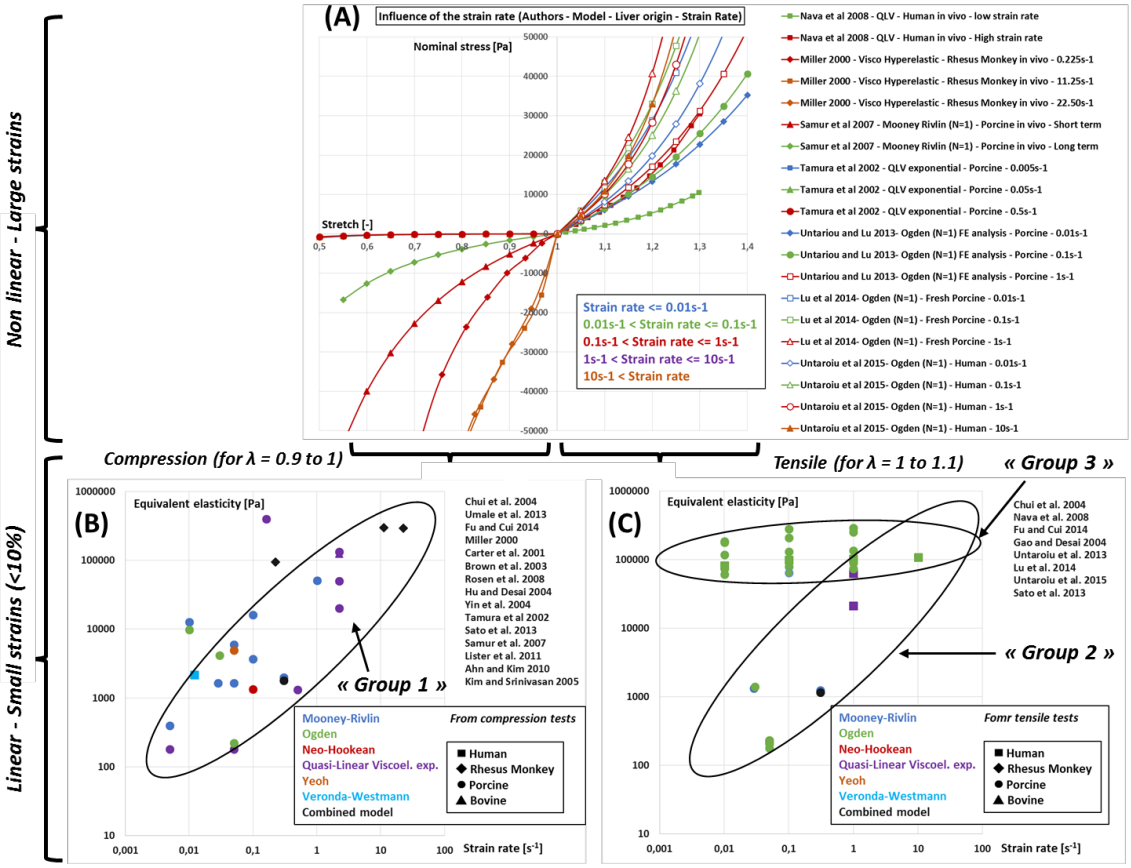

Figure 2: First Piola-Kirchhoff (nominal) stress as a function of stretch for the main studies dealing with the influence of the strain rate on the liver nonlinear modeling in tensile/compression uniaxial testing (A). From this graph, the equivalent elasticity values are deduced as a function of the strain rate for the linear part (strains < 10%) in compression (B) and tensile (C) for the nonlinear models proposed in the literature (color scale).

liver mechanical response, depending on the application of the model (such as computer assisted surgery - low strain rates, or abdominal impact trauma - high strain rates).

3.2.3. Anisotropy

Most of the biological soft tissues, such as muscle and brain, are composed of fibers, which results in highly anisotropic mechanical properties and behavior. Accounting anisotropy in the tissue model is a critical issue. However, divergences can be observed in the literature about the inclusion of anisotropy in the nonlinear models of healthy hepatic tissue. While high transverse isotropy has been related in both tensile and compression by Chui *et al.* in 2007 (with a factor 2 between longitudinal and transverse stiffness at 20% strain), the large majority of the studies observe and model the liver tissue as isotropic (Chui et al., 2007). In 2011, no significant differences were found by Pervin *et al.* in the nonlinear compressive response obtained from bovine specimens along the liver surface and perpendicular to it for a large range of strain rates (Pervin

et al., 2011). Similarly, most of the experimental results and models in the literature indicate isotropic behavior of liver tissue.

3.2.4. Inter-species variations

In spite of major morphological variations, most of the nonlinear constitutive laws of hepatic tissue have been identified from animal specimens (rhesus monkey (Miller, 2000), swine (Tamura et al., 2002; Brown et al., 2003; Sato et al., 2013), and bovine (Pervin et al., 2011)). Whatever the species is, the hepatic tissue has been shown to have highly nonlinear stress-strain behavior and most of the current liver models include the use of animal tissue to simulate human organs. However, the disparity between the experimental protocols related in the literature does not allow to highlight significant interspecies differences to be highlighted in the nonlinear behavior of the liver tissue. A comparison between the models identified using similar protocols by Untaroiu *et al.* in 2013 and 2015 shows that the human liver tissue is 1.34-1.48 and 1.49-1.73 times stiffer than the porcine hepatic tissue at 10% and 20% strain, respectively (Untaroiu and Lu, 2013; Untaroiu et al., 2015b).

3.2.5. Characterization of the Glissons capsule

While no difference have been observed by testing hepatic tissue in presence and in absence of the capsule by some authors (Chui et al., 2007), the capsule has specific characteristics, which are thought to result in modification of the global nonlinear mechanical behavior of the liver. The addition of the capsule to the simulation process more accurately reflects the boundary conditions present in a real *in vivo* organ (Lister et al., 2011). The capsule has been shown to be mechanically isotropic at a mesoscale. The capsule has a great influence on the fracture of the liver, involving ultimate strain between 47% and 50.5% and ultimate load of 0.3 N/mm for the entire organ (Brunon et al., 2010, 2011). Based on identification of the third-order Ogden model and assuming incompressibility, isotropy and strain rate independence, the small strains and large strains elastic moduli have been obtained at 8.22 and 48.15 MPa by Umale *et al.*, i.e. significantly stiffer than the hepatic tissue alone (Umale et al., 2011), confirming the importance of including the capsule to simulate the response of the entire liver.

3.3. Finite Element Models of the Liver

The development of liver finite element models at the organ scale, and not only at tissue scale, has been driven initially by surgery simulation applications, thus requiring near real-time computations. In this context, approaches often assumed a linear elastic behavior (Cotin et al., 2000) discretized on linear tetrahedron finite elements, which naturally leads to solving a linear system of equations whose inverse eventually could be precomputed (James and Pai, 1999).

Since linear elastic materials are not suitable for large displacements, several authors in the computer animation community have proposed corotational elastic models (Suwelack et al., 2012; Courtecuisse et al., 2010), in which linear elastic stiffness matrices are rotated for each element. While coping with finite strains, those models are restricted by the material linearity. More realistic soft tissue deformations may be obtained by resorting to hyperelastic materials minimizing a continuum strain energy. For real-time computation, early approaches have been based on St. Venant Kirchhoff materials (Delingette and Ayache, 2004) which exhibit a linear stress-strain relationship. Significant speed-up can be obtained by using reduced basis of deformation (Barbič and James, 2005), proper generalized decomposition (Niroomandi et al., 2013) or by grouping expressions on edges, triangles, and tetrahedra (Picinbono et al., 2003) when discretized on linear tetrahedra.

For general hyperelastic materials, several authors have relied on the finite element method to simulate soft-tissue deformation with explicit time integration schemes (Speidel et al., 2011). For instance, Miller *et al.* (Miller et al., 2006) have developed the total Lagrangian explicit dynamic (TLED) algorithm with neo-Hookean materials. This approach has been combined with Prony series to model viscoelasticity and has been implemented on graphics processing units (GPU) (Taylor et al., 2009) to reach real-time computations. However the main limitation of this approach is that it relies on explicit time integration schemes, which greatly simplify the update at each time step but requires small time steps to keep the computation stable, especially for stiff materials.

4. A Porous Viscohyperelastic Finite Element Model of the Liver

As discussed Section 3, hepatic tissue material law is highly dependent on the strain rate for low and high deformations. The dependence in high deformation should be taken into account by adding a viscosity component to the hyperelasticity, while the dependence in low deformation is mainly because of porosity. We chose to combine a hyperelastic model of the hepatic tissue with viscosity and porosity as described in (Marchesseau et al., 2010). Fig.3(Left) shows schematically how these three components interact within a physically based model. The model is made of an isochoric part containing the viscosity and hyperlasticity in series, and a volumetric part to account for the extracellular fluid present in the liver, acting in parallel to the isochoric component. The porosity component introduces the fluid pressure as an additional state variable. In the next sections, the individual components and underlying variables are described in details.

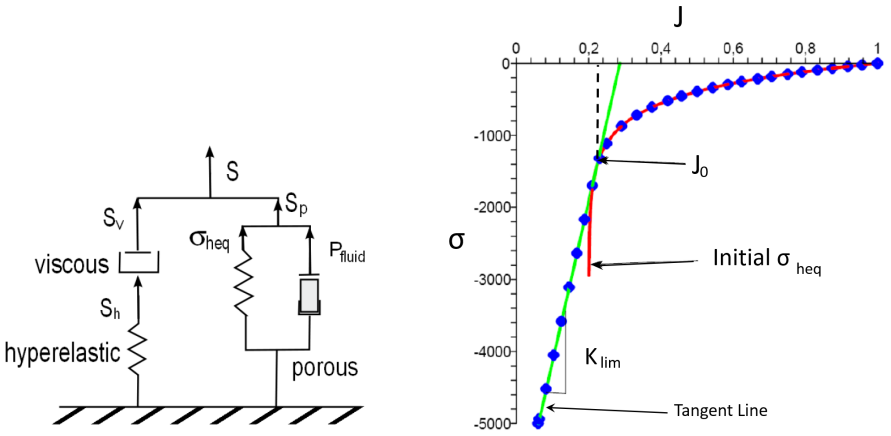

Figure 3: (Left) Representation of the constitutive model combining viscosity, hyperelasticity and porosity. (Right) Representation of the static Cauchy stress before and after substitution leading to the final dotted curve. Here $f_w = 0.8$.

4.1. Optimised Assembly of Finite Elements for Hyperelastic Materials

4.1.1. Limitations of the classical FEM approach

Finite Element models for hyperelasticity usually require significant computation times when solved by implicit time integration schemes. The objective of this section is to introduce a more

optimised discretization method suitable for all hyperelastic materials that increases the computational efficiency when assembling force vectors and stiffness matrices, necessary to the resolution of the FEM. To discretize the liver geometry, we use tetrahedral linear finite elements built from 3D medical imaging. Linear tetrahedra have constant strain which implies using a single integration point and simplifies the computation of shape functions gradient. However, the developed optimizations could be easily extended to other elements, such as linear hexahedra elements or high-order tetrahedra.

As described in previous chapters, any hyperelastic material is fully determined by its strain energy function W, which describes the amount of energy necessary to deform the material. Based on variational principles (Zienkiewicz and Taylor, 2000), classical approaches involve the expensive computation of the second Piola-Kirchhoff (SPK) stress tensor $\mathbf{S}$ and the elasticity tensor $N_{ijkl} = 2\frac{\partial S_{ij}}{\partial C_{kl}}$ where $\mathbf{C}$ is the right Cauchy-Green deformation tensor. This discretization method suffers three limitations:

- The formulation and the computation of the SPK stress tensor $\mathbf{S}$ and the elasticity tensor $\hat{\mathbf{N}}$ can be fairly complex. Indeed, the first and second derivatives of the Jacobian $J = det\mathbf{F}$ with respect to $\mathbf{C}$ is nontrivial and involves the inversion of $\mathbf{C}$. This makes the expression of the derivatives of the invariants of $\mathbf{C}$, $\bar{I}_1$ and $\bar{I}_2$ particularly cumbersome and therefore computationally expensive to evaluate (see (Weiss et al., 1996) for details).

- The strain-displacement matrix $\hat{\mathbf{B}}$ involved in the force and stiffness calculations combines two terms: the deformation gradient $\mathbf{F}$ and the gradient of the shape functions D_i. The former changes at each iteration, while the latter is constant. For basic hyperelastic materials for which the elasticity tensor $\hat{\mathbf{N}}$ is constant or nearly constant, this is not optimal; a better choice would be to isolate the deformation gradient and to combine the shape vectors with the elasticity tensor.

- The classical FEM formulation of hyperelastic material cannot cope with nearly flat ($J \equiv 0$) or even inverted tetrahedra ($J < 0$). Although such deformation are non physical and do not represent a meaningful configuration, in interactive simulations, such cases of extreme compression can be met due to contact with rigid objects or to nonphysical user-defined gestures. For instance, if the user-interface is not equipped with force-feedback, the tool controlled by the user can undergo nonplausible trajectories. To cope with this, it is important to propose a hyperelastic material that can handle nearly flat tetrahedra.

4.1.2. Multiplicative jacobian energy decomposition

Our original discretization method addresses at least partially, the three limitations of classical FEM. It is important to note that the approach developed in this section is completely equivalent to the classical FEM one but leads to more efficient assembly of the matrices before resolution of the system. First, instead of computing the force (f) and stiffness matrix ($\mathbf{K}$) using the first and second derivative of the energy with respect to $\mathbf{C}$ (leading respectively to $\mathbf{S}$ and $\hat{\mathbf{N}}$), we compute them directly by deriving the energy with respect to the nodal position (Q_i):

$$f_i = -\left(\frac{\partial W}{\partial Q_i}\right)^T \text{ and } \mathbf{K}_{ij} = \left(\frac{\partial^2 W}{\partial Q_j \partial Q_i}\right)$$

Then, our approach consists of three separate contributions:
i) Decomposition of strain energy

We propose to write the strain energy functions as a sum of terms

$$W^k = g^k(\tilde{I})h^k(J)$$

or a function of it (for instance its exponential for Fung's law), where $\tilde{I} = (I_1, I_2, I_4...)$. The purpose is to decouple the invariants of the right Cauchy-Green deformation tensor $\mathbf{C}$ from the Jacobian J in the strain energy. This allows us to avoid matrix inversions and complex derivative expressions. Therefore, g^k is independent of J, and its derivative will not involve any matrix inversions. This decomposition applies to many hyperlastic laws such as, Veronda Westmann, Arruda-Boyce, St. Venant Kirchhoff, neo-Hookean, Ogden, and Mooney Rivlin for the liver, or Costa's exponential law (Costa et al., 2001) for the cardiac muscle. Using this decomposition of strain energy enables complex material formulation to be computed more efficiently with only a sum of reasonably simple terms and no matrix inversions. Once the decomposition is done, getting $h^{k\prime}(J) = \frac{dh^k}{dJ}$ requires a 1D derivation, and getting $\mathbf{S}^k = 2\frac{\partial g^k(\tilde{I})}{\partial \mathbf{C}}$ requires combining well-known derivatives of the invariants, such as $\frac{\partial I_1}{\partial \mathbf{C}} = \mathbf{Id}$ or $\frac{\partial I_2}{\partial \mathbf{C}} = \mathbf{Id}I_1 - \mathbf{C}$. The nodal forces therefore require only the inputs of the gradient of the shape functions D_i, and the strain energy terms $h^k, h^{k\prime}, g^k$ and $\mathbf{S}^k$ (see (Marchesseau et al., 2010) for full derivation):

$$f_i = -V_0 \sum_k \left(h^{k\prime}(J) g^k(\tilde{I}) \left(\frac{\partial J}{\partial Q_i} \right)^T + h^k(J) \mathbf{F}\, \mathbf{S}^k\, D_i \right)$$

ii) Formulation of the stiffness matrix

Implicit time integration schemes require the computation of the tangent stiffness matrix at each time step. This naturally involves elasticity tensors computed as the derivative of $\mathbf{S}^k$ for each tetrahedron and at each time step. Multiplicative Jacobian Energy Decomposition (MJED) leads to far simpler expressions of those tensors because $\mathbf{S}^k$ is independent of J. Furthermore, in many common materials, the term containing those elasticity tensors can be precomputed. The full expression of the stiffness matrix includes six terms:

$$\frac{\partial^2 W(T_P)}{\partial Q_i \partial Q_j} = V_0 \sum_k (\mathbf{G}^k + \mathbf{H}^k + \mathbf{I}^k + \mathbf{\Lambda}^k + \mathbf{M}^k + \mathbf{R}^k)$$

where

$$\begin{cases} \mathbf{G}^k = \left(\frac{\partial h^{k\prime}(J)}{\partial Q_j} \right)^T \frac{\partial J}{\partial Q_i} g^k(\tilde{I}) & \mathbf{H}^k = h^{k\prime}(J) \frac{\partial}{\partial Q_j} \frac{\partial J}{\partial Q_i} g^k(\tilde{I}) & \mathbf{I}^k = h^{k\prime}(J) \left(\frac{\partial g^k(\tilde{I})}{\partial Q_j} \right)^T \frac{\partial J}{\partial Q_i} \\ \mathbf{\Lambda}^k = \left(\frac{\partial h^k(J)}{\partial Q_j} \right)^T D_i^T\, \mathbf{S}^k\, \mathbf{F}^T & \mathbf{M}^k = h^k(J)\, D_i^T\, \mathbf{S}^k \left(\frac{\partial \mathbf{F}^T}{\partial Q_j} \right)^T & \mathbf{R}^k = h^k(J) \left(\frac{\partial \mathbf{S}^k}{\partial Q_j} D_i \right)^T \mathbf{F}^T \end{cases}$$

We focus in more details on the term involving the third-order tensor $\frac{\partial \mathbf{S}^k}{\partial Q_j}$:

$$\mathbf{R}^k = h^k(J) \left(\frac{\partial \mathbf{S}^k}{\partial Q_j} D_i \right)^T \mathbf{F}^T$$

The third-order tensor $\frac{\partial \mathbf{S}^k}{\partial Q_j}$ is computed through the chain rule with the the elasticity tensor $\frac{\partial \mathbf{S}^k}{\partial \mathbf{C}}$. Instead of representing the fourth-order tensor $\frac{\partial \mathbf{S}^k}{\partial \mathbf{C}}$ through 6×6 matrices, we define it through

its application $\frac{\partial \mathbf{S}^k}{\partial \mathbf{C}} : \mathbf{H}$ on any symmetric matrix $\mathbf{H}$. More precisely, we define the scalars (β_l^k, δ_l^k), and 3×3 symmetric matrices $(\mathbf{A}_l^k, \mathbf{B}_l^k)$ such that:

$$\frac{\partial \mathbf{S}^k}{\partial \mathbf{C}} : \mathbf{H} = \sum_l \beta_l^k \mathbf{A}_l^k \, \mathbf{H}\mathbf{A}_l^k + \delta_l^k (\mathbf{H} : \mathbf{B}_l^k)\mathbf{B}_l^k$$

where $\mathbf{A} : \mathbf{B} = tr(\mathbf{B}^T\mathbf{A})$ for any two matrices $\mathbf{A}, \mathbf{B}$. Finally, the term $\mathbf{R}^k$ is found to be a combination of two terms:

$$h^k(J)\mathbf{F}\, \mathbf{L}_l^k(i,j)\mathbf{F}^T \text{ and } h^k(J)\mathbf{F}\, \mathbf{U}_l^k(i,j)\mathbf{F}^T$$

where $\mathbf{L}_l^k(i,j)$ and $\mathbf{U}_l^k(i,j)$ are linear matrices:

$$\begin{cases} \mathbf{L}_l^k(i,j) = \beta_l^k \left(\mathbf{A}_l^k \, D_i \otimes D_j \, \mathbf{A}_l^k + \mathbf{A}_l^k (D_j \cdot \mathbf{A}_l^k \, D_i) \right) \\ \mathbf{U}_l^k(i,j) = \delta_l^k \left(\mathbf{B}_l^k \, D_j \otimes D_i \, \mathbf{B}_l^k \right) \end{cases}$$

This formulation leads to an optimization for the assembly of the stiffness matrix for two reasons. First, only scalars and 3×3 symmetric matrices are involved in the computation. Second, except for the Ogden model, the matrices $\mathbf{A}_l^k$ and $\mathbf{B}_l^k$ are constant, and therefore matrices $\mathbf{L}_l^k(i,j)$ and $\mathbf{U}_l^k(i,j)$ can be precomputed for each tetrahedron before the simulation.

iii) Coping with highly compressed elements

In case of high compression, the volumetric terms $h^k(J)$ in the strain energy become dominant. This makes the stiffness matrix singular and thus leads to numerically unstable computations because there are an infinity number of deformed configurations leading to the same value of J. In order to cope with this, (Teran et al., 2005) perform an SVD decomposition of the deformation gradient matrix. To avoid this computationally expensive decomposition, we propose instead to *regularize* the term $\mathbf{G}^k = h^{k''}(J)\, g^k(\tilde{I}) \, \frac{\partial J}{\partial Q_j} \otimes \frac{\partial J}{\partial Q_i}$ by replacing it with the following expression:

$$\mathbf{G}^k = h^{k''}(J) g^k(\tilde{I}) \left((1-\epsilon) \frac{\partial J}{\partial Q_j} \otimes \frac{\partial J}{\partial Q_i} + \epsilon \frac{\partial J}{\partial Q_j} \cdot \frac{\partial J}{\partial Q_i} \mathbf{Id} \right)$$

The closer ϵ is to 1 the closer the $\mathbf{G}^k$ matrix is to a diagonal matrix. In practice, we set $\epsilon = (1 - J)$ if $0 \leq J \leq 1$, $\epsilon = 0$ if $J \geq 1$ and $\epsilon = 1$ if $J \leq 0$. In all cases, the trace of the regularized matrix is equal to the trace of the original matrix. By regularizing only the stiffness matrix, we still minimize the strain energy and therefore do not change the nature of the hyperelastic material. With this technique, it is even possible to handle inverted elements when the strain energy remains finite as $J = 0$.

One limitation of the MJED method is that is does not directly compute the (first or) second Piola Kirchhoff stress tensor $\mathbf{S} = 2\frac{W}{\partial \mathbf{C}}$. If such stress tensors are required, then they need to be computed at extra cost (see below).

4.2. Viscohyperelasticity Based on Prony Series

To model accurately the viscoelasticity of the liver, we propose to rely on Prony series (Taylor et al., 2009). This consists in adding to the hyperelastic SPK stress tensor now denoted ${}^{\mathbf{h}}\mathbf{S}$ some time dependent stresses. This time dependence is given by $\alpha(t) = \alpha_\infty + \sum_i \alpha_i e^{-t/\tau_i}$ with the condition $(\alpha_\infty + \sum_i \alpha_i) = 1$. The viscohyperelastic SPK tensor noted ${}^{\mathbf{v}}\mathbf{S}$ can then be written as:

$${}^{\mathbf{v}}\mathbf{S} = \int_0^t \alpha(t-t') \frac{\partial \, {}^{\mathbf{h}}\mathbf{S}}{\partial t'} dt' = {}^{\mathbf{h}}\mathbf{S} - \sum_i \gamma_i \quad \text{where} \quad \gamma_i = \int_0^t \alpha_i (1 - e^{(t'-t)/\tau_i}) \frac{\partial \, {}^{\mathbf{h}}\mathbf{S}}{\partial t'} dt'$$

After a discretization over time this results in the recursive formula between time $n-1$ and time n:

$$\gamma_i^n = a_i\, {}^{\mathbf{h}}\mathbf{S}^n + b_i \gamma_i^{n-1} \text{ where } a_i = \frac{\Delta t \alpha_i}{\Delta t + \tau_i} \text{ and } b_i = \frac{\tau_i}{\Delta t + \tau_i}$$

Δt is the time step used for discretization and has to be the same as the time step for any solvers during the simulation. To combine the Prony series with our optimized hyperelastic formulation, we therefore need to compute the total hyperelastic SPK stress tensor ${}^{\mathbf{h}}\mathbf{S}^n$. This is done for each time step n (dropping the index for clarity) by computing the inverse deformation gradient:

$${}^{\mathbf{h}}\mathbf{S} = \mathbf{F}^{-1}\left(\sum_k (f^{k\prime}(J) g^k(\tilde{I}) J\mathbf{F}^{-T} + f^k(J)\mathbf{F}\, {}^{\mathbf{h}}\mathbf{S}^k)\right) \quad \text{where} \quad \mathbf{F}^{-1} = \left(\sum_{l=1}^4 P_l \otimes \frac{\partial J}{\partial Q_l}\right)/J$$

The viscohyperelastic nodal forces ${}^v f$ are therefore related to the hyperelastic ones ${}^h f$ by

$${}^v f_i = {}^h f_i + V_0 \mathbf{F} \sum_i \gamma_i D_i$$

Moreover, once we have γ_i^{n-1}, the stiffness matrix is also slightly updated at each time n from its hyperelastic formulation ${}^{\mathbf{h}}\mathbf{K}$:

$${}^{\mathbf{v}}\mathbf{K}_{ij}^n = {}^{\mathbf{h}}\mathbf{K}_{ij}^n \left(1 - \sum_k a_k\right) - V_0 D_j^T \left(\sum_k b_k \gamma_k^{n-1}\right) D_i \mathbf{Id}$$

Adding the viscous properties through the Prony series does not have a significant impact on the total computation times despite the evaluation of the time dependent stresses γ_i^n and $\mathbf{F}^{-1}$.

4.3. Poroelasticity

We follow Kerdok's porosity model (Kerdok, 2006) and consider the liver as a fluid-filled sponge. This model is made of a volumetric component (represented by σ_{Heq} (Fig.3) and a fluid phase with variable P_{fluid}). The volumetric component is governed by Hencky's elasticity (Xiao and Chen, 2002), in which the Cauchy stress depends on the proportion of free-fluid (e.g. blood, water) in the liver parenchyma in the reference configuration (r_w) and the effective volumetric Jacobian $J^* = (r_w + J - 1)/r_w$ by:

$$\sigma_{Heq} = K_0\, r_w\, ln(J^*)$$

where K_0 is the bulk modulus of the material. With this model, when J get close to $1 - r_w$, the solid phase of the liver is completely compressed and the resulting stress is infinite. To avoid instabilities due to this infinite stress, we substitute σ_{Heq} when $J \leq J_0$ by its tangent curve at J_0 (see Fig.3(Right)). We set $J_0 = 1 - r_w + K_0/K_{lim}$ where K_{lim} is a bulk modulus and represents the slope of the tangent.

The fluid phase of the liver also applies some volumetric stresses due to the transient response of the fluid through the porous liver parenchyma. A straightforward way of modeling the porous behavior is through the linear Darcy's law. In this setting, variation of fluid pressure P_{fluid} is governed by the variation of volume change and a diffusive process:

$$\frac{1}{K_{lim}} \dot{P}_{fluid} = \kappa \nabla^2 P_{fluid} - \frac{\dot{J}}{J}$$

where κ is the permeability parameter. In Kerdok's model, the permeability κ is a function of J, but we propose to keep it constant to decrease its computational cost.

Finally, the total Cauchy stress response in the volumetric part is defined by summing the solid and the fluid terms:

$$\sigma_p = \sigma_{heq}\mathbf{Id} - P_{fluid}\mathbf{Id}$$

The Cauchy stress is translated as a poroelastic force:

$${}^{p}f_i = -\sigma_p \left(\frac{\partial J}{\partial Q_i}\right)^T V_0$$

added to the viscohyperelastic forces. The additional stiffness matrix, which is regularized similarly to previously described in Section 4.1.2 iii), is given as:

$${}^{\mathbf{p}}\mathbf{K}_{ij} = V_0 \left(\frac{\partial \sigma_p}{\partial J} \left(\frac{\partial J}{\partial Q_j}\right)^T \left(\frac{\partial J}{\partial Q_i}\right) + \sigma_p \frac{\partial^2 J}{\partial Q_j \partial Q_i} \right)$$

Adding porosity to the model decreases slightly the computational efficiency due to the use of a semi-implicit resolution scheme.

5. Results

5.1. MJED validation

First, we compared the computation time between the MJED and the classical FEM method, referred to as Standard FEM, implemented in SOFA[1]. The results are given in Fig.4. We measured the time elapsed for the computation of the nodal forces and the stiffness matrices averaged during 100 iterations. For a more detailed differentiation between force and stiffness assembly computation, the reader is referred to (Marchesseau et al., 2010). We simulated the deformation of a cube with 20,700 tetrahedra and 4300 nodes. For all laws implemented, the proposed strategy is definitely more efficient than the standard FEM, up to five times as fast for St. Venant Kirchhoff material.

Second, the accuracy of the MJED computation was compared against the open source software FEBio (version 1.1.7)[2] where several elastic and hyperelastic materials are implemented, and against analytical solutions for simple cube model. The mean relative difference is around 10^{-6} for every models tested. Moreover, a mesh convergence study was performed to evaluate the trade-off between accuracy and speed on several meshes. Dividing a mesh 20 times only increases the accuracy by 1% while multiplying the computation time by 10.

5.2. Rheological Testing on Porcine Liver: Experimental Materials and Methods

To calibrate the viscoelastic parameters of our liver model, tests were performed on porcine livers. Dynamic viscoelastic behavior of hepatic tissue was investigated using *in vitro* dynamic mechanical analysis (DMA) in rotating shear. Tests were carried out on liver cylindrical-shaped samples coming from five adult pigs (weighting between 25 and 35 kg). Immediately after hepatectomy performed on anesthetized animals, entire livers were stored in an insulated container

[1] SOFA is an Open Source medical simulation software available at www.sofa-framework.org

[2] FEBio is an opensource software package for FE analysis available at mrl.sci.utah.edu

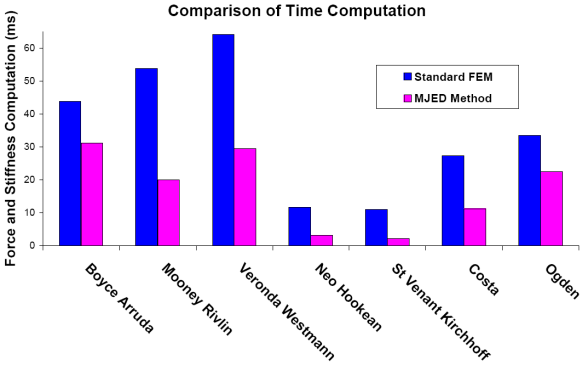

Figure 4: Comparison of the computation times of nodal forces and stiffness matrices between two different discretization methods averaged over 100 iterations.

at 6°C surrounded by ice. Cylindrical hepatic samples of 20 mm diameter and 41 mm thick were cut and tested within 6 hours *postmortem* time. To avoid mechanical difference because of samples location, four samples were tested for each of right, middle, and left liver lobes. Hepatic tissue is considered as isotropic. At least 60 samples were tested (5 animals x 3 lobes x 4 samples).

Dynamic Strain Sweep tests and Dynamic Frequency Sweep tests were performed on a dedicated stress-controlled AR2000 (TA-Instruments, New Castle, DE, USA) rheometer in a parallel-plate configuration. A precompression of 5mN was applied and sand paper was fixed to the rheometer plates to ensure grip with tested sample.

Dynamic Strain Sweep. Those tests aim at giving linearity limit of material's elasticity. The sweep covers strain range from 0.01% to 20%, which is sufficient, according to the literature. Measurement of both storage G' and loss G'' shear moduli as functions of shear strain showed that the linearity domain extends up to 1%-2% of deformation.

Dynamic Frequency Sweep. These experiments were carried out in the linear viscoelastic strain range of the sample ($\gamma_0 = 0.1\%$) with frequencies ranging from 0.1 to 4 Hz. From the 60 tested samples, we display the mean curves (Fig.5, mean ± standard deviation values) of the storage G' and loss G'' shear moduli, which correspond to the real and imaginary parts of the complex shear modulus $G^*(\omega) = G'(\omega) + iG''(\omega)$, respectively. From these results the Dynamic Modulus G can be obtained as a function of the frequency or function of the time, and the viscoelastic behavior can be modeled after fitting a generalized Maxwell model with two modes of relaxation to those measurements:

$$G(t) = G_0(g_\infty + g_1 e^{-t/\tau_1} + g_2 e^{-t/\tau_2})$$

where $G_\infty = G_0\ g_\infty$ is the equilibrium modulus, g_1, g_2, τ_1, τ_2 are model relaxation parameters such as $g_\infty + g_1 + g_2 = 1$. The parameters are given Table 2. Our estimated initial and equilibrium shear moduli were 770 and 333 Pa, respectively. While corresponding to one of the lowest values related in the literature, these parameters are in agreement with most of the studies dealing with hepatic tissue rheological testing at surgical strain rates. (Lister et al., 2011; Tamura et al., 2002; Kim and Srinivasan, 2005; Ahn and Kim, 2010; Fu and Chui, 2014)

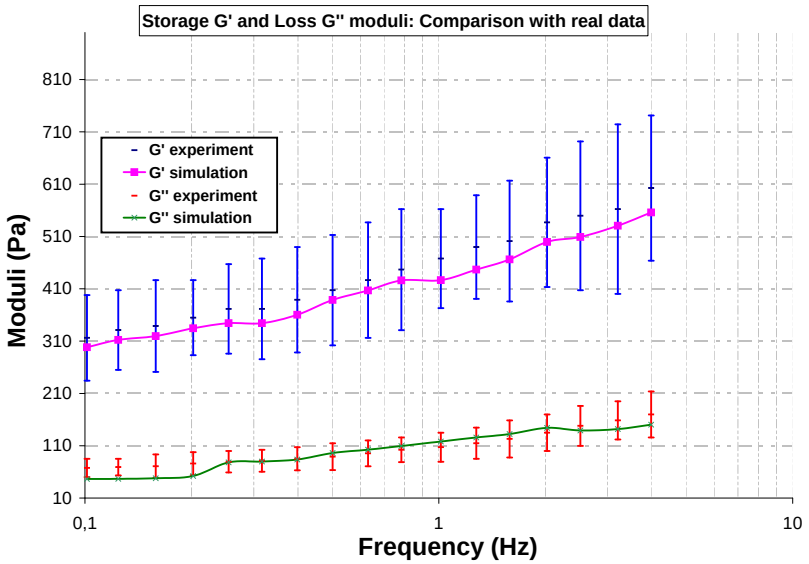

Figure 5: Comparison of the simulated values with the data obtained by DMA testing. The moduli are given on a log-log scale. The material is St Venant Kirchhoff, similar values are found for other materials.

Viscosity					Porosity			
$G_0(Pa)$	$g_1(Pa)$	$\tau_1(s)$	$g_2(Pa)$	$\tau_2(s)$	r_w	$K_0(Pa)$	$K_{lim}(kPa)$	$\kappa(m^4/Ns)$
770	0.235	0.27	0.333	0.03	0.5	400	2.2	20

Table 2: Values of the parameters identified from the DMA Tests for the viscosity and from the literature for the porosity.

5.3. Model Parameter Fitting From Experiments

From the rheological experiments described in the previous section, we derive the initial shear modulus G_0 required in the hyperelastic term and the Prony series parameters required in the viscous term. To check that those parameters are indeed valid, we propose in this section to compare *insilico* simulations with the performed *in vitro* rheological tests. The rheological tests were performed in the linearity domain isolating the viscous properties and therefore eliminating the influence of the chosen hyperelastic material. First, we check that the linearity domain for our hyperelastic materials matches the ones observed in the dynamic strain sweep experiments. We simulate a cylinder in extension in SOFA for several longitudinal stresses and estimate the associated strains. The linearity limit corresponds to the one given by experiments ($1\% - 2\%$).

Second, dynamic frequency sweep tests have been simulated using similar geometries and boundary conditions to the DMA tests. An oscillating torque (amplitude M) is applied on a small cylinder (radius $r = 10mm$, height $h = 4mm$) at various frequencies ω. The amplitude of the torque is chosen so as to stay in the linear domain. The angle of rotation θ of the cylinder is measured as a function of time. This angle describes a sinusoidal curve which follows the torque amplitude with a shifted phase δ. Specific constraint is applied on the top cylinder nodes to enforce a pure rotation of those nodes (as to reproduce the pure grip of sand paper).

Using similar calculation of stress and strain as for the rheometry experiments, we can esti-

mate the values of the Storage and Loss moduli to be compared with experimental data. It can be seen in Fig.5 that the simulation manages to capture the viscous behavior of the liver for small deformations with a mean relative error of 5%. By comparison with the constitutive laws in both compression and tension from the literature, this behavior observed in shear is in good agreement with most of the studies at similar strain rates (ranging from 0.008 to 0.250 s-1) (Lister et al., 2011; Tamura et al., 2002; Kim and Srinivasan, 2005; Ahn and Kim, 2010; Fu and Chui, 2014). By the use of strain rates similar to those from most of the surgical applications, this results confirms the capability of our model to simulate the liver response during surgical interventions.

5.4. Liver Simulations

To describe the influence of each component in the complete model several simulations were performed in which the hyperelastic material used was a fifth-order Arruda-Boyce (Arruda and Boyce, 1993) based on Kerdok's (Kerdok, 2006) observations that the parenchyma was best represented by a 8-chain rubber like elastic material. The liver mesh was segmented from a CT image and meshed with the GHS3D software (1240 vertices and 5000 tetrahedra). A Euler implicit time integration scheme is used and the linear equations are solved with a conjugated gradient algorithm. As boundary conditions, several nodes of the liver are fixed along the vena cava and suspensive ligament. The liver deforms under the constant action of gravity applied through the whole simulation such as to overpass the linearity limit of the material. All computations were performed on a laptop PC with a Intel Core Duo processor at 2.80 GHz.

(i) Influence of the viscous component

Adding viscosity to hyperelasticity increases the amplitude of the oscillations as the material becomes less stiff. Contrary to an essentially hyperelastic model, the final state is really different from the initial state (see Fig.6 (Bottom)). Indeed, the use of Prony series leads to a multiplication of the SPK tensor by $1 - \sum a_k$ at infinite time. The frame rate is around 9 FPS against 10 FPS for hyperelasticity alone. However the implicit integration scheme allows larger time step (0.3 s for instance) which makes the real-time interaction possible. High amount of extension and compression are possible, which may be somewhat unrealistic, therefore the porous component is necessary to control the amount of viscosity.

(ii) Porohyperelastic simulation

We have implemented the porous component in parallel to the hyperelastic component using parameters based on Kerdok's (Kerdok, 2006) experimental data, shown Table 2. The simulated fluid pressure field during the deformation is shown in Fig.6 (Top) as a color map (see online version), ranging from dark blue (initial pressure) to red (highest pressure). Highest pressure in the fluid occurs when the liver is compressed either by gravity (diffusion starts at the top), either by elastic reaction (diffusion starts from the bottom).

(iii) Complete model

Adding porosity to viscohyperelasticity prevents the liver from having unrealistic large deformations. The resulting deformation differs from the simple use of a stiffer hyperelastic material by its non-isotropic and time-dependent behavior. The addition of this component decreases the computational efficiency (6 FPS) since a semi-implicit integration scheme is used for the porous component. However, because of the fast variation of the explicit term $\dot{J}/J$, the time step has to be decreased to 0.15 s. On our laptop PC, the simulation is still fluid enough to allow user interactions.

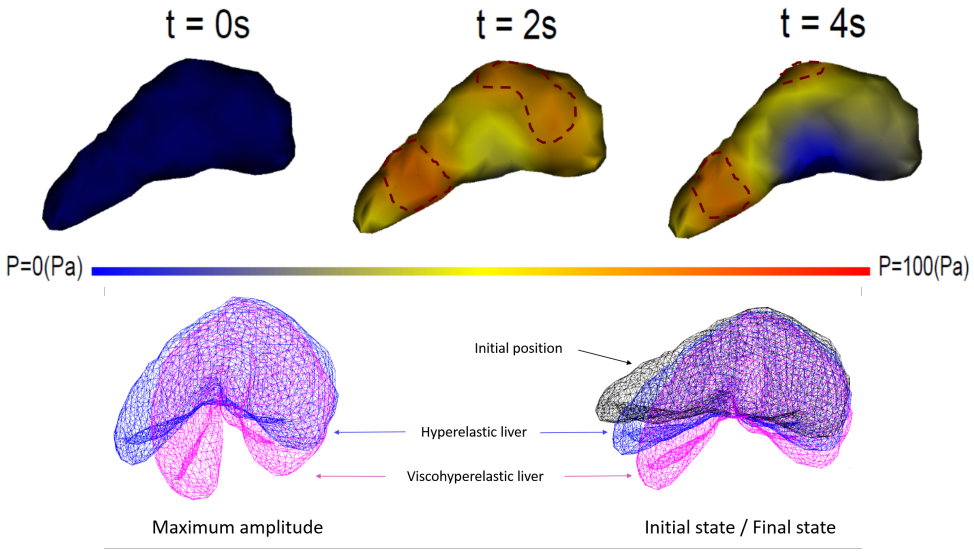

Figure 6: (Top) Pressure field of the porous component on a liver under gravity, during one oscillation (dotted lines highlight the areas with the highest pressure). (Bottom) Addition of viscosity to hyperelasticity: comparison of the maximum amplitudes and final states.

6. Discussion and Perspectives

Liver biomechanics has been quite extensively studied in prior work, and this chapter provides a synthetic view of hyperelastic material parameters that were fit on various rheological experiments. It appears that strain rate has a major influence on tissue behavior thus hinting for the use of viscohyperelastic or even viscoporohyperelastic models. However, the variety of experimental conditions (*ex vivo* vs. *in vivo*, strain rate, considered species, etc.) makes it difficult to provide a precise quantitative characterization of liver mechanics. Clearly, significant advances in this direction can only be obtained by a coordinated effort by the scientific community to standardize the experimental process and the modeling choices.

Furthermore, liver mechanical properties are strongly influenced by the physiological conditions of the subject. For instance, liver fibrosis is fairly common in chronic liver diseases, and hepatic stiffness has been shown to increase with the staging liver fibrosis and with the METAVIR scoring system (Castéra et al., 2005) because of the excessive accumulation of collagen fibers. Fatty liver disease (hepatic steatosis) also translates into a significant increase in liver stiffness (Huwart et al., 2008). Elastography imaging techniques based on ultrasound (Gennisson et al., 2013; Fatemi and Greenleaf, 1998) or magnetic resonance imaging (Muthupillai et al., 1995) are being developed to provide patient-specific maps of linear mechanical parameters (mainly elastic or viscoelastic shear moduli) of the main abdominal organs. These noninvasive measurements are currently limited to small deformations but open new avenues for the design of patient-specific biomechanical models. In particular, they could be useful to provide quantitative information about the boundary conditions of the liver with respect to neighboring organs, of which little is known.

Finally, global finite element models of the liver have been developed mainly for medical

applications and in particular for surgery training and therapy guidance. In both cases, fast or real-time simulations are required, thus leading to fairly simplified mechanical models. In this paper, a porous viscohyperelastic model was presented with a fast assembly of the stiffness matrix leading to optimized performances. This approach can be further improved by taking into account the mechanical resistance because of the large vessels inside the liver and more appropriate boundary conditions. In addition, with the development of non invasive elastography and MR or ultrasound intraoperative imaging, it is foreseeable that such mechanical models could be validated and personalized with regional parameters, and not only global ones.

References

Ahn, B. and Kim, J. (2010). Measurement and characterization of soft tissue behavior with surface deformation and force response under large deformations. *Medical Image Analysis*, 14(2):138–148.

Arruda, E. M. and Boyce, M. C. (1993). A three-dimensional constitutive model for the large stretch behavior of rubber elastic materials. *Journal of the Mechanics and Physics of Solids*, 41(2):389–412.

Bano, J., Hostettler, A., Nicolau, S., Cotin, S., Doignon, C., Wu, H. S., Huang, M. H., Soler, L., and Marescaux, J. (2012). Simulation of pneumoperitoneum for laparoscopic surgery planning. In *Medical Image Computing and Computer-Assisted Intervention - MICCAI 2012 - 15th International Conference, Nice, France, October 1-5, 2012, Proceedings, Part I*, pages 91–98.

Barbič, J. and James, D. L. (2005). Real-time subspace integration for St. Venant-Kirchhoff deformable models. *ACM TOG (SIGGRAPH 2005)*, 24(3):982–990.

Brown, J. D., Rosen, J., Kim, Y. S., Chang, L., Sinanan, M. N., and Hannaford, B. (2003). In-vivo and in-situ compressive properties of porcine abdominal soft tissues. *Studies in Health Technology and Informatics*, pages 26–32.

Brunon, A., Bruyere-Garnier, K., and Coret, M. (2010). Mechanical characterization of liver capsule through uniaxial quasi-static tensile tests until failure. *Journal of biomechanics*, 43(11):2221–2227.

Brunon, A., Bruyere-Garnier, K., and Coret, M. (2011). Characterization of the nonlinear behaviour and the failure of human liver capsule through inflation tests. *Journal of the mechanical behavior of biomedical materials*, 4(8):1572–1581.

Carter, F. J., Frank, T. G., Davies, P. J., McLean, D., and Cuschieri, A. (2001). Measurements and modelling of the compliance of human and porcine organs. *Medical Image Analysis*, 5(4):231–236.

Castéra, L., Vergniol, J., Foucher, J., Bail, B. L., Chanteloup, E., Haaser, M., Darriet, M., Couzigou, P., and de Ldinghen, V. (2005). Prospective comparison of transient elastography, fibrotest, apri, and liver biopsy for the assessment of fibrosis in chronic hepatitis c. *Gastroenterology*, 128(2):343 – 350.

Chatelin, S., Oudry, J., Périchon, N., Sandrin, L., Allemann, P., Soler, L., and Willinger, R. (2011). In vivo liver tissue mechanical properties by transient elastography: Comparison with dynamic mechanical analysis. *Biorheology*, 48(2):75–88.

Chui, C., Kobayashi, E., Chen, X., Hisada, T., and Sakuma, I. (2004). Combined compression and elongation experiments and non-linear modelling of liver tissue for surgical simulation. *Medical and Biological Engineering and Computing*, 42(6):787–798.

Chui, C., Kobayashi, E., Chen, X., Hisada, T., and Sakuma, I. (2007). Transversely isotropic properties of porcine liver tissue: experiments and constitutive modelling. *Medical & biological engineering & computing*, 45(1):99–106.

Costa, K. D., Holmes, J. W., and McCulloch, A. D. (2001). Modelling cardiac mechanical properties in three dimensions. *Philosophical Transactions of the Royal Society of London A: Mathematical, Physical and Engineering Sciences*, 359(1783):1233–1250.

Cotin, S., Delingette, H., and Ayache, N. (2000). A hybrid elastic model allowing real-time cutting, deformations and force-feedback for surgery training and simulation. *The Visual Computer*, 16(8):437–452.

Courtecuisse, H., Jung, H., Allard, J., Duriez, C., Lee, D. Y., and Cotin, S. (2010). Gpu-based real-time soft tissue deformation with cutting and haptic feedback. *Progress in Biophysics and Molecular Biology*, 103(23):159 – 168. Special Issue on Biomechanical Modelling of Soft Tissue Motion.

Delingette, H. and Ayache, N. (2004). Soft tissue modeling for surgery simulation. In *Computational Models for the Human Body*, pages 453–550. Elsevier.

Fatemi, M. and Greenleaf, J. F. (1998). Ultrasound-stimulated vibro-acoustic spectrography. *Science*, 280(5360):82–85.

Fu, Y. and Chui, C. (2014). Modelling and simulation of porcine liver tissue indentation using finite element method and uniaxial stress–strain data. *Journal of biomechanics*, 47(10):2430–2435.

Fu, Y., Chui, C., and Teo, C. (2013). Liver tissue characterization from uniaxial stress–strain data using probabilistic and inverse finite element methods. *Journal of the mechanical behavior of biomedical materials*, 20:105–112.

Fung, Y. (1967). Elasticity of soft tissues in simple elongation. *American Journal of Physiology–Legacy Content*, 213(6):1532–1544.

Gao, Z. and Desai, J. P. (2010). Estimating zero-strain states of very soft tissue under gravity loading using digital image correlation. *Medical image analysis*, 14(2):126–137.

Gennisson, J.-L., Deffieux, T., Fink, M., and Tanter, M. (2013). Ultrasound elastography: principles and techniques. *Diagnostic and interventional imaging*, 94(5):487–495.

Haouchine, N., Cotin, S., Peterlík, I., Dequidt, J., Sanz-Lopez, M., Kerrien, E., and Berger, M. (2015). Impact of soft tissue heterogeneity on augmented reality for liver surgery. *IEEE Trans. Vis. Comput. Graph.*, 21(5):584–597.

Hu, T. and Desai, J. P. (2003). A biomechanical model of the liver for reality-based haptic feedback. In *Medical Image Computing and Computer-Assisted Intervention-MICCAI*, pages 75–82. Springer, Berlin/Heidelberg.

Hu, T. and Desai, J. P. (2004). Characterization of soft-tissue material properties: large deformation analysis. In *Medical Simulation*, pages 28–37. Springer, Berlin/Heidelberg.

Huwart, L., Sempoux, C., Vicaut, E., Salameh, N., Annet, L., Danse, E., Peeters, F., ter Beek, L. C., Rahier, J., Sinkus, R., et al. (2008). Magnetic resonance elastography for the noninvasive staging of liver fibrosis. *Gastroenterology*, 135(1):32–40.

James, D. L. and Pai, D. K. (1999). ArtDefo accurate real time deformable objects. In *Computer Graphics (SIGGRAPH)*, pages 65–72.

Jordan, P., Socrate, S., Zickler, T., and Howe, R. (2009). Constitutive modeling of porcine liver in indentation using 3d ultrasound imaging. *Journal of the mechanical behavior of biomedical materials*, 2(2):192–201.

Kerdok, A. E. (2006). *Characterizing the Nonlinear Mechanical Response of Liver to Surgical Manipulation*. PhD thesis, Harvard University.

Kim, J. and Srinivasan, M. A. (2005). Characterization of viscoelastic soft tissue properties from in vivo animal experiments and inverse fe parameter estimation. In *Medical Image Computing and Computer-Assisted Intervention–MICCAI*, pages 599–606. Springer, Berlin/Heidelberg.

Kobayashi, Y., Watanabe, H., Hoshi, T., Kawamura, K., and Fujie, M. G. (2012). *Soft Tissue Biomechanical Modeling for Computer Assisted Surgery*, chapter Viscoelastic and Nonlinear Liver Modeling for Needle Insertion Simulation, pages 41–67. Springer Berlin Heidelberg, Berlin, Heidelberg.

Lister, K., Gao, Z., and Desai, J. P. (2011). Development of in vivo constitutive models for liver: application to surgical simulation. *Annals of biomedical engineering*, 39(3):1060–1073.

Liu, Z. and Bilston, L. (2002). Large deformations shear properties of liver tissue. *Biorheology*, 39(6):735–742.

Lu, Y.-C., Kemper, A. R., and Untaroiu, C. D. (2014). Effect of storage on tensile material properties of bovine liver. *Journal of the mechanical behavior of biomedical materials*, 29:339–349.

Marchesseau, S., Heimann, T., Chatelin, S., Willinger, R., and Delingette, H. (2010). Fast porous visco-hyperelastic soft tissue model for surgery simulation: Application to liver surgery. *Progress in biophysics and molecular biology*, 103(2):185–196.

Miller, K. (2000). Constitutive modelling of abdominal organs. *Journal of biomechanics*, 33(3):367–373.

Miller, K., Joldes, G., Lance, D., and Wittek, A. (2006). Total lagrangian explicit dynamics finite element algorithm for computing soft tissue deformation. *Communications in Numerical Methods in Engineering*, 23:121–134.

Muthupillai, R., Lomas, D., Rossman, P., Greenleaf, J., Manduca, A., and Ehman, R. (1995). Magnetic resonance elastography by direct visualization of propagating acoustic strain waves. *Science*, 269(5232):1854–1857.

Nava, A., Mazza, E., Furrer, M., Villiger, P., and Reinhart, W. (2008). In vivo mechanical characterization of human liver. *Medical image analysis*, 12(2):203–216.

Nava, A., Mazza, E., Haefner, O., and Bajka, M. (2004). Experimental observation and modelling of preconditioning in soft biological tissues. In *Medical Simulation*, pages 1–8. Springer, Berlin.

Nickel, F., Brzoska, J. A., Gondan, M., Rangnick, H. M., Chu, J., Kenngott, H. G., Linke, G. R., Kadmon, M., Fischer, L., and Muller-Stich, B. P. (2015). Virtual reality training versus blended learning of laparoscopic cholecystectomy: a randomized controlled trial with laparoscopic novices. *Medicine (Baltimore)*, 94(20):e764.

Nicolle, S., Vezin, P., and Palierne, J.-F. (2010). A strain-hardening bi-power law for the nonlinear behaviour of biological soft tissues. *Journal of biomechanics*, 43(5):927–932.

Niroomandi, S., Gonzlez, D., Alfaro, I., Bordeu, F., Leygue, A., Cueto, E., and Chinesta, F. (2013). Real-time simulation of biological soft tissues: a pgd approach. *International Journal for Numerical Methods in Biomedical Engineering*, 29(5):586–600.

Oktay, O., Zhang, L., Mansi, T., Mountney, P., Mewes, P. W., Nicolau, S., Soler, L., and Chefd'Hotel, C. (2013). Biomechanically driven registration of pre- to intra-operative 3d images for laparoscopic surgery. In *Medical Image Computing and Computer-Assisted Intervention - MICCAI 2013 - 16th International Conference, Nagoya, Japan, September 22-26, 2013, Proceedings, Part II*, pages 1–9.

Ottensmeyer, M. (2002). Tempest 1-d: an instrument for measuring solid organ soft tissue properties. *Experimental Techniques*, 26(3):48–50.

Pervin, F., Chen, W. W., and Weerasooriya, T. (2011). Dynamic compressive response of bovine liver tissues. *Journal of*

the mechanical behavior of biomedical materials, 4(1):76–84.

Picinbono, G., Delingette, H., and Ayache, N. (2003). Non-Linear Anisotropic Elasticity for Real-Time Surgery Simulation. *Graphical Models*, 65(5):305–321.

Plantefève, R., Peterlik, I., Haouchine, N., and Cotin, S. (2015). Patient-specific biomechanical modeling for guidance during minimally-invasive hepatic surgery. *Annals of Biomedical Engineering*, 44(1):139–153.

Raghunathan, S., Evans, D., and Sparks, J. L. (2010). Poroviscoelastic modeling of liver biomechanical response in unconfined compression. *Annals of biomedical engineering*, 38(5):1789–1800.

Roan, E. and Vemaganti, K. (2007). The nonlinear material properties of liver tissue determined from no-slip uniaxial compression experiments. *Journal of biomechanical engineering*, 129(3):450–456.

Rosen, J., Brown, J. D., De, S., Sinanan, M., and Hannaford, B. (2008). Biomechanical properties of abdominal organs in vivo and postmortem under compression loads. *Journal of Biomechanical Engineering*, 130(2):021020.

Samur, E., Sedef, M., Basdogan, C., Avtan, L., and Duzgun, O. (2007). A robotic indenter for minimally invasive measurement and characterization of soft tissue response. *Medical Image Analysis*, 11(4):361–373.

Sato, F., Yamamoto, Y., Ito, D., Antona-Makoshi, J., Ejima, S., Kamiji, K., and Yasuki, T. (2013). Hyper-viscoelastic response of perfused liver under dynamic compression and estimation of tissue strain thresholds with a liver finite element model. In *IRCOBI conference*.

Simpson, A. L., Dumpuri, P., Jarnagin, W. R., and Miga, M. I. (2012). *Soft Tissue Biomechanical Modeling for Computer Assisted Surgery*, chapter Model-Assisted Image-Guided Liver Surgery Using Sparse Intraoperative Data, pages 7–40. Springer Berlin Heidelberg, Berlin, Heidelberg.

Speidel, S., Roehl, S., Suwelack, S., Dillmann, R., Kenngott, H., and Mueller-Stich, B. (2011). Intraoperative surface reconstruction and biomechanical modeling for soft tissue registration. In *Proc. Joint Workshop on New Technologies for Computer/Robot Assisted Surgery*, pages 0–0.

Suwelack, S., Röhl, S., Dillmann, R., Wekerle, A.-L., Kenngott, H., Müller-Stich, B., Alt, C., and Speidel, S. (2012). *Computational Biomechanics for Medicine: Deformation and Flow*, chapter Quadratic Corotated Finite Elements for Real-Time Soft Tissue Registration, pages 39–50. Springer New York, New York, NY.

Tamura, A., Omori, K., Miki, K., Lee, J. B., Yang, K. H., and King, A. I. (2002). Mechanical characterization of porcine abdominal organs. *Stapp car crash journal*, 46:55–69.

Taylor, Z., Comas, O., Cheng, M., passenger, J., hawkes, D., Atkinson, D. ., and Ourselin, S. (2009). On modelling of anisotropic viscoelasticity for soft tissue simulation: numerical solution and gpu execution. *medical image Analysis*, 13:234–244.

Teran, J., Sifakis, E., Blemker, S. S., Ng-Thow-Hing, V., Lau, C., and Fedkiw, R. (2005). Creating and simulating skeletal muscle from the visible human data set. *IEEE Transactions on Visualization and Computer Graphics*, 11(3):317–328.

Umale, S., Chatelin, S., Bourdet, N., Deck, C., Diana, M., Dhumane, P., Soler, L., Marescaux, J., and Willinger, R. (2011). Experimental in vitro mechanical characterization of porcine glisson's capsule and hepatic veins. *Journal of biomechanics*, 44(9):1678–1683.

Umale, S., Deck, C., Bourdet, N., Dhumane, P., Soler, L., Marescaux, J., and Willinger, R. (2013). Experimental mechanical characterization of abdominal organs: liver, kidney & spleen. *Journal of the mechanical behavior of biomedical materials*, 17:22–33.

Untaroiu, C. D. and Lu, Y.-C. (2013). Material characterization of liver parenchyma using specimen-specific finite element models. *Journal of the mechanical behavior of biomedical materials*, 26:11–22.

Untaroiu, C. D., Lu, Y.-C., Siripurapu, S. K., and Kemper, A. R. (2015a). Modeling the biomechanical and injury response of human liver parenchyma under tensile loading. *Journal of the Mechanical Behavior of Biomedical Materials*, 41:280 – 291.

Untaroiu, C. D., Lu, Y.-C., Siripurapu, S. K., and Kemper, A. R. (2015b). Modeling the biomechanical and injury response of human liver parenchyma under tensile loading. *Journal of the mechanical behavior of biomedical materials*, 41:280–291.

Vappou, J. (2012). Magnetic resonance- and ultrasound imaging- based elasticity imaging methods: A review. *Critical Reviews¢ in Biomedical Engineering*, 40(2).

Weiss, J., Maker, B., and Govindjee, S. (1996). Finite element implementation of incompressible, transversely isotropic hyperelasticity. *Computer methods in applied mechanics and engineering*, 135:107–128.

Xiao, H. and Chen, L. (2002). Hencky's elasticity model and linear stress-strain relations in isotropic finite hyperelasticity. *Acta Mechanica*, 157:51–60.

Yin, H., Sun, L., Wang, G., and Vannier, M. W. (2004). Modeling of elastic modulus evolution of cirrhotic human liver. *Biomedical Engineering, IEEE Transactions on*, 51(10):1854–1857.

Zienkiewicz, C. and Taylor, R. (2000). *The Finite Element Method, Volume 2 : Solid Mechanics*. Butterworth-Heinemann, London.